



**HAL**  
open science

## Surface acoustic wave confinement inside uncorrelated distributions of subwavelength scatterers

Thibault Deletang, Adnane Noual, Bernard Bonello, Roman Buisine, Yan Pennec, Bahram Djafari-Rouhani

► **To cite this version:**

Thibault Deletang, Adnane Noual, Bernard Bonello, Roman Buisine, Yan Pennec, et al.. Surface acoustic wave confinement inside uncorrelated distributions of subwavelength scatterers. *Journal of Applied Physics*, 2023, 134 (24), pp.134, 243102-1. 10.1063/5.0173970 . hal-04435488

**HAL Id: hal-04435488**

**<https://hal.science/hal-04435488>**

Submitted on 16 May 2024

**HAL** is a multi-disciplinary open access archive for the deposit and dissemination of scientific research documents, whether they are published or not. The documents may come from teaching and research institutions in France or abroad, or from public or private research centers.

L'archive ouverte pluridisciplinaire **HAL**, est destinée au dépôt et à la diffusion de documents scientifiques de niveau recherche, publiés ou non, émanant des établissements d'enseignement et de recherche français ou étrangers, des laboratoires publics ou privés.



Distributed under a Creative Commons Attribution 4.0 International License

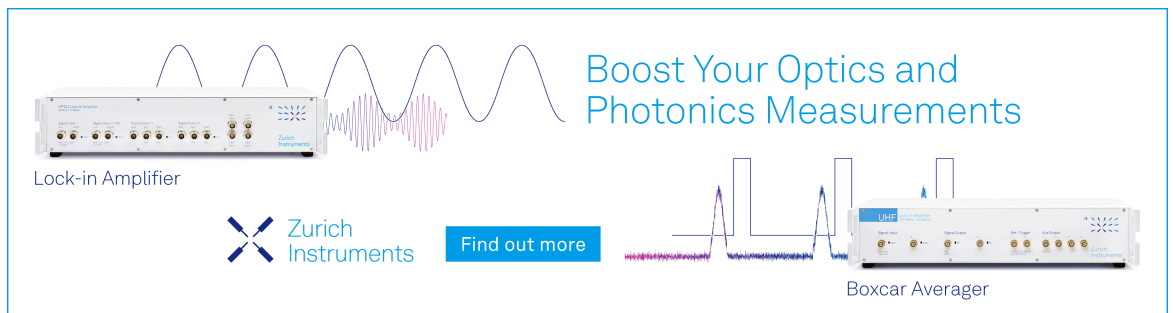
RESEARCH ARTICLE | DECEMBER 22 2023

# Surface acoustic wave confinement inside uncorrelated distributions of subwavelength scatterers <sup>F</sup>

Thibault Deletang <sup>ORCID</sup>; Adnane Noual <sup>ORCID</sup>; Bernard Bonello <sup>ORCID</sup>; Roman Buisine; Yan Penneç <sup>ORCID</sup>; Bahram Djafari-Rouhani <sup>ORCID</sup>


 Check for updates

*J. Appl. Phys.* 134, 243102 (2023)  
<https://doi.org/10.1063/5.0173970>



Boost Your Optics and Photonics Measurements

Lock-in Amplifier

 Zurich Instruments






[Find out more](#)

Boxcar Averager

# Surface acoustic wave confinement inside uncorrelated distributions of subwavelength scatterers

Cite as: J. Appl. Phys. **134**, 243102 (2023); doi: [10.1063/5.0173970](https://doi.org/10.1063/5.0173970)  
Submitted: 22 September 2023 · Accepted: 29 November 2023 ·  
Published Online: 22 December 2023



Thibault Deletang,<sup>1</sup>  Adnane Noual,<sup>2,3</sup>  Bernard Bonello,<sup>1,a)</sup>  Roman Buisine,<sup>2</sup> Yan Pennec,<sup>2</sup>   
and Bahram Djafari-Rouhani<sup>2</sup> 

## AFFILIATIONS

<sup>1</sup>Institut des NanoSciences de Paris, Sorbonne Université, Paris 75005, France

<sup>2</sup>Département de Physique, Institut d'Electronique, de Microélectronique et Nanotechnologie, Université de Lille, Villeneuve d'Ascq 59655, France

<sup>3</sup>Laboratoire de Physique, de la Matière et des Rayonnements, Université Mohammed Premier, Oujda 60000, Morocco

<sup>a)</sup>Author to whom correspondence should be addressed: [bernard.bonello@insp.jussieu.fr](mailto:bernard.bonello@insp.jussieu.fr)

## ABSTRACT

We report an experimental study of surface acoustic wave (SAW) localization and propagation in random metasurfaces composed of Al scatterers using pump–probe spectroscopy. Thanks to this technique, wideband high frequency acoustic modes are generated, and their dynamical propagation directly from inside of the media with a high (micrometric) spatial resolution is enabled. During SAW propagation, part of the acoustic wavefront energy is trapped within free areas between the scatterers, acting as cavities. The spectral content of the localized modes of a few GHz is found to depend on the shape and size of the cavities but also on the landscape seen by the wave during its propagation before arriving inside them. The experimental results are supported by numerical simulations using the finite element method. This study is the phononic part of a more global research on the co-localization of elastic and optical waves on random metasurfaces, with the main objective of enhancing the photon–phonon interaction. Applications could range from the design of acousto-optic modulators to ultrasensitive sensors.

© 2023 Author(s). All article content, except where otherwise noted, is licensed under a Creative Commons Attribution (CC BY) license (<http://creativecommons.org/licenses/by/4.0/>). <https://doi.org/10.1063/5.0173970>

## I. INTRODUCTION

The study of optical and acoustic waves in complex media has considerably evolved over the last decades. Among them, the study of artificial periodic structures such as phononic, photonic crystals, acoustic, and electromagnetic metamaterials has largely contributed to breaking conventional physical limitations. These properties paved the way for the design of engineered disordered systems with remarkable spectral or topological properties,<sup>1</sup> ultra-broad band light absorption,<sup>2</sup> sound insulation,<sup>3</sup> subwavelength focusing,<sup>4–8</sup> optical or acoustic clocking,<sup>9,10</sup> or more recently, demonstration of anomalous reflections/transmissions and topologic insulators.<sup>11,12</sup> Actually, most of these properties need the support of phononic and photonic crystals that exhibit local resonances, giving rise to one or several forbidden bands at frequencies well below the Bragg range. Since Anderson's pioneering work on electrons,<sup>13</sup> particular

attention has been paid to localization phenomena in random disordered systems, stimulating studies such as the strong localization of acoustic and electromagnetic waves in random media.<sup>14</sup> In 1984, John theoretically showed an electromagnetic mobility edge in a disordered medium, where an anomalous decrease of energy transmission rises due to Anderson localization fluctuation as the photon frequency approaches a certain critical value.<sup>15</sup> In 2008, Hu *et al.* reported the localization of ultrasound in the Anderson sense in a 3D elastic medium consisting of a three-dimensional granular network of aluminum beads.<sup>16</sup> An interesting so-called 3D transverse localization manifested by a cut-off in the transverse spreading of multiple scattered waves has been shown. Over the last few decades, a great deal of research efforts have been devoted to investigate wave localization properties in the broad sense in disordered media.<sup>17–25</sup> In the phononic domain, the introduction of disorder

16 May 2024 13:35:41

has been mentioned in relation to its effect on bandgap properties. It has been shown that the latter can be extended further beyond the absolute frequency band of the ordered crystal; this is achieved through the disorder introduction in the phononic system inducing strong Anderson localization, which results in a much wider absolute bandgap.<sup>26</sup> Moreover, when physical contact between scatterers is established, unexpected responses may appear, often linked to the percolation limit.<sup>27</sup> In that regard, the response of a disordered arrangement of scatterers where physical contact between them can occur, deserves careful analysis. This is why the behavior of random structures has been subjected to intense research in recent years.<sup>28</sup> These efforts have led Fernández-Marín *et al* to show a controllable anomalous localization effect, beyond the standard Anderson localization, using a Lévy-type distribution in a 1D waveguide structure operating in the microwaves range.<sup>29</sup> More recently, random arrays of nano-antennas have been introduced as a means of avoiding the diffraction losses inherent in single- or multiple-size periodic absorbers.<sup>30,31</sup> To date, there is plenty of experimental and/or theoretical evidence of acoustic wave localization already reported such as in phononic structures typically made of solid beads<sup>16,32</sup> or disordered elastic rods.<sup>33</sup> Nonetheless, in all these systems, the localized elastic wave frequencies are limited to low range domains, very rarely exceeding ~tens of MHz. However, studies on the localization effects of high-frequency elastic waves are still lacking. In that context, we report in this work, an experimental study of high-frequency (~GHz) surface acoustic wave (SAW) localization in random metasurfaces composed of Al scatterers. Specifically, the metasurfaces consist of an assembly of several thousands of aluminum pillars arranged randomly on a 100 nm thin film, also made of aluminum, deposited on a semi-infinite silica substrate. The SAW generation, detection, and dynamical monitoring are performed using pump-probe spectroscopy. The random distribution of Al pillars obeys the Poisson statistics, where unfilled areas with different shapes referred to as cavities, appear out of the disorder during fabrication. We provide experimental evidence of GHz-SAW localization in such cavities, which is supported by numerical simulations based on the finite element method. In particular, we show how the trapped SAW wavelengths systematically relate to the cavity dimensions as if the localized waves were effective eigenmodes. The reported findings are meant to help investigate enhanced acousto-optical coupling in random metasurfaces where SAW and optical resonances are co-localized,<sup>34</sup> with a view to design acousto-optical modulators or ultrasensitive sensors.

The paper is organized as follows. In Sec. II, the fabricated sample's geometry and the experimental setup are presented. Then, in Sec. III, we give the key experimental results regarding SAW trapping/localization in various shaped cavities, while Sec. IV provides the numerical data supporting the experimental results. Conclusions are summarized in Sec. V.

## II. SAMPLE GEOMETRY AND EXPERIMENTAL SETUP

The random distribution is composed of Al pillars that act as weak scatterers when the spectral content of the propagating SAW is far from their resonances. However, the incident wave will be subject to multiple scattering. The spatial distribution of the scatterers' centers has been calculated to obey a Poisson statistic,

despite a hard sphere condition (of 10 nm) that is imposed for manufacturing considerations. To ensure that the resonant frequencies of the pillars are not excited by the SAW, their dimensions have been chosen so that the first bending mode and compression mode are above ~1.8 GHz [see Fig. 12(e) in the Appendix], i.e., a diameter of  $\varphi \sim 320$  nm for a height of  $h = 200$  nm. The pillars are directly fabricated on a thin Al layer of thickness  $e \sim 100$  nm deposited on a SiO<sub>2</sub> substrate using a physical vapor deposition (PVD) technique. The Al layer is known to be a very good transducer layer for picosecond acoustic technique since it has a small penetration depth and a high reflecting coefficient in the near IR, ensuring a good signal-to-noise ratio (SNR).<sup>35</sup> The SiO<sub>2</sub> substrate was chosen for its mechanical impedance close to that of aluminum allowing the generation of a low dispersive surface acoustic mode.

The process of fabricating the scatterers on the Al layer involves several steps. The first step consists of depositing a resin (of a thickness greater than that targeted for the pillars), which is then irradiated by an E-beam (electron lithography) technique whose electron concentration can be modified as required. This dose, which corresponds to the density of charges per unit area (in  $\mu\text{C cm}^{-2}$ ), has a major impact on the diameter of the pillars actually obtained in relation to what was targeted. The higher the concentration is, the more the surface area will be irradiated and the larger the diameter of the scatterers will be, so it is necessary to perform several dose tests to know what diameter will be obtained at the end of the fabrication process, compared to the desired dimensions. Once the pillar patterns are inscribed in the resin, Al is deposited on the sample using PVD to fill the holes obtained by electron lithography. Finally, the sample is placed in a chemical solution that attacks the resin remaining on the sample, in order to bring out the pillars: this is the lift-off phase, at the end of which, only the Al pillars deposited in the lithographed regions remain on the sample. A wide field scanning electronic microscope (SEM) image of one of the samples thus obtained is given in Fig. 1(a). There are approximately 20 000 scatterers distributed on a  $120 \times 12 \mu\text{m}^2$  area in order to have a pillar spatial surface density  $\rho = 10\%$  ensuring strong multiple scattering effects.<sup>36</sup>

These random distributions have been generated using a hard sphere condition small enough to keep the scatterers' positions uncorrelated. On each scatterer, a 10 nm exclusion radius was placed to avoid interpenetration of the pillars since the manufacturing processes used ensure this condition, as long as the distance between the two edges is greater than about 20 nm. As shown in Fig. 1(b), only a marginal proportion of scatterers fabricated that way has percolated. Since the resonant frequencies of the scatterers are not excited, this low number of percolated pillars does not affect our study.

Considering the dimensions of the samples, a method of generation and detection of very high frequency acoustic waves is necessary for their study, while the classical methods using piezoelectric transducers do not satisfy this condition. The picosecond acoustic technique is then ideal since it allows to generate and detect via pulsed lasers (with a repetition rate  $T_R = 12.5$  ns) acoustic modes of a few  $\mu\text{m}$  in wavelength, making the study of nanostructures possible. The excitation of the acoustic wave is done by means of a laser focused on a thin Al layer (100 nm). Then, a transfer of energy from photons to electrons takes place, which causes the generation of an acoustic stress that propagates, due to the relaxation

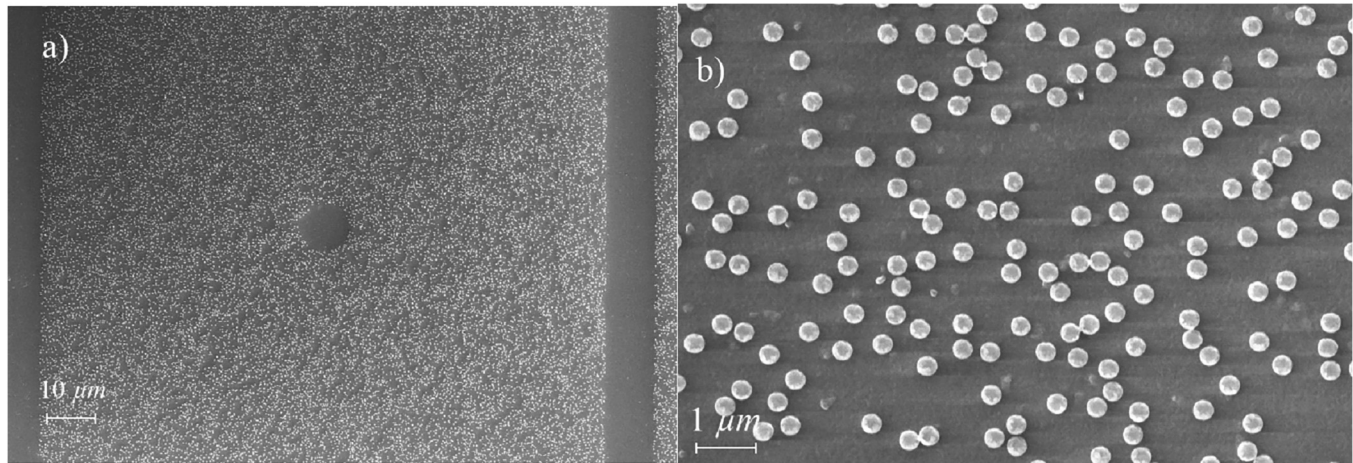


**FIG. 1.** SEM images of (a) wide field and (b) zoom of a random distribution of Al scatterers. The pillars of diameter  $\varphi \sim 320$  nm and height  $h \sim 200$  nm are distributed on an area of  $120 \times 120 \mu\text{m}^2$  and are fabricated on an Al layer of thickness  $e \sim 100$  nm itself deposited on a  $\text{SiO}_2$  substrate.

of the electrons. The acoustic wave can be detected via the out-of-plane displacement (orthogonal to its direction of propagation) by an amplitude of a few pm on the surface of the sample, by measuring the interferences between two laser beams. These two beams, pump (generation) and probe (detection), can be spatially shifted, thanks to a delay line, which then enables us to observe wave propagation over several ns with a resolution of a few ps. The relative variations of reflectivity related to the propagation of the SAW, governed by the out-of-plane displacement  $u$  at these frequencies, are detected by means of a Sagnac interferometer chosen for its high mechanical stability. The signal reflected back by the sample is then sent to a differential photodiode connected to a lock-in detection scheme. A  $4f$  imaging system also allows to image the wave propagating through the metasurface on a maximum area of  $100 \times 100 \mu\text{m}^2$  with a spatial resolution equivalent to the width of the focal spot at the output of a  $\times 100$  microscope objective lens with a large numerical aperture ( $\text{NA} = 0.9$ ). The acoustic modes thus generated—called Sezawa modes—are very wideband since all frequencies between 100 MHz and 1.8 GHz are excited (for the  $\text{SiO}_2$  substrate), which corresponds to wavelengths of a few  $\mu\text{m}$ , taking into account their propagation velocity on the surface of the substrate. The latter has been characterized on the samples in the absence of scatterers and their dispersion has been shown experimentally to be negligible over the propagation distances investigated. Moreover, the propagation velocity on the metasurfaces is  $3600 \text{ ms}^{-1}$  and the minimum wavelength in the generated elastic pulse is  $\sim 2 \mu\text{m}$ , more than one order of magnitude larger than the radius of the scatterers.

### III. EXPERIMENTAL RESULTS AND DISCUSSION

During the propagation on the surface of the substrate, the acoustic wave interacts with each of the scatterers of the distribution that will act as secondary sources. This multitude of scattered waves will interact together and lead to constructive interference

phenomena that can be detected with our current experimental setup. A  $50 \times 50 \mu\text{m}^2$  scan of the propagation of a surface wave through a random distribution with a scatterer concentration of  $\rho = 10\%$  is given in Fig. 2. For a fixed pump–probe delay, the excitation zone is located at the top right of the image. We see two acoustic wave fronts separated in time by  $T_R = 12.5$  ns, which corresponds to the laser repetition rate, with a constellation of areas that are over-vibrating several ns after the passage of the wave, and randomly distributed in the metasurface. By superimposing scatterers' positions on the image, we can see that the majority of these zones are located in glades free of pillars. This means that during its propagation, part of the acoustic wave energy is trapped inside the pillar-free areas that continue to vibrate during several ns. A very large range of zones with very different shapes and sizes among the disordered distributions fabricated have been identified and can be sometimes assimilated to simple geometric shapes, which we will call here cavities. This study focuses on the resonance of individual cavities exhibiting circular and rectangular shapes. To this end, the probe beam is placed in the pillar-free zone of interest and is separated from the pump by  $10 \mu\text{m}$ . Then, their paths are desynchronized, thanks to a delay line, in order to study the vibrations of that zone over time, after the passage of the SAW through it. That way, the wavefront that has been propagating in the distribution has left the cavity of interest since 0.5 ns before the measurement starts. The circular cavities studied and identified by a gray circle with their close surroundings are given in Fig. 3(a). The spectra calculated from the temporal measurements in the three associated cavities are summarized in Fig. 3(b), where the reference spectral content of the acoustic signal in the sample in the absence of scatterers is overlaid and represented as a dashed-dotted line.

The results reveal that despite the large spectral width of the reference signal, only a small part of the frequencies that have passed through the cavities remain inside and that the main frequency seems to depend on their dimensions with respect to the direction of propagation. For the sake of clarity, the experimental spectra have

16 May 2024 13:35:41

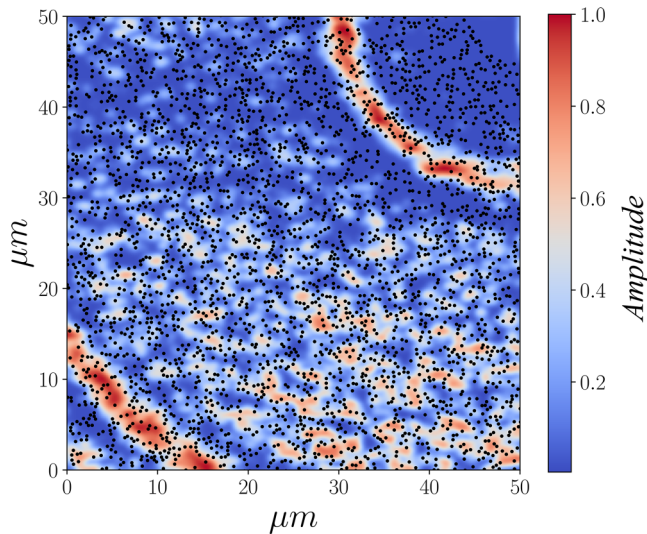


**FIG. 2.**  $50 \times 50 \mu\text{m}^2$  scan of the surface acoustic wave propagation through a random distribution of density  $\rho = 10\%$  for a fixed pump-probe delay, the excitation is located in the upper right part of the image. Two elastic wave fronts are seen, separated by  $T_R = 12.5$  ns with a large number of over-vibrating areas between them. The black dots superimposed on the scan represent the positions of the scatters. The color scale on the right corresponds to the squared amplitude of the out-of-plane displacement. Note that the lower contrast in the upper part of the image results from experimental constraints, essentially the stability of optical settings over the entire measurement period which generally lasts several tens of minutes.

been self-normalized and vertically displaced in order to highlight the frequency shift. Indeed, the smaller these dimensions are, the more the main mode detected inside is of high frequency. The velocity of the surface acoustic waves in the absence of scatterers has been measured at  $v_{\text{SiO}_2} \sim 3600$  m/s and shown to propagate without dispersion on the distance scales studied. Several successive wavefront measurements report that their amplitudes decay following a  $1/\sqrt{r}$  law, with  $r$  the propagation distance, which reflects the energy distribution on a corona, characteristic of a Rayleigh wave. A detailed study of the attenuation of the elastic wave propagating in the metasurface is beyond the scope of this work. However, it can be noted here that wavefront damping results from various causes, including radiation in the volume due to scatterers, localization of elastic energy in certain free surfaces between scatterers, viscoelastic effects, dispersion, etc., whose relative contributions are extremely difficult to measure. The absence of dispersion allows us to approximate the wavelength of the principal modes present in the corresponding cavities, taking into account their resonance frequencies. The main modes obtained are  $\lambda_1 = 2.6 \mu\text{m}$ ,  $\lambda_2 = 2.4 \mu\text{m}$ , and  $\lambda_3 = 2.2 \mu\text{m}$  and allow to establish a clear link between the characteristic dimensions of the cavities and the main modes present inside since the larger the latter, the lower the frequency of the mode will be.

The main mode detected in a cavity depends not only on its dimensions but also on its geometrical shape. In that regard, the rest of this study focused on a rectangular cavity of dimension  $2 \times 5 \mu\text{m}^2$ , highlighted by the red area in Fig. 4(a). In the same way

as for the previous measurements, the pump is placed at  $10 \mu\text{m}$  from the probe, which is located in the center of the cavity. Time measurements of the out-of-plane displacement  $u(t)$  obtained in this experimental configuration, following the passage of the surface acoustic wave in the cavity, are given with the associated (Fourier transform) spectrum in Figs. 4(b) and 4(c), respectively. The latter shows that vibrations persist for 4 ns without significant attenuation and that it corresponds to a main mode of wavelength  $\lambda = 2 \mu\text{m}$ , so the equivalence between the dimensions of the cavity and the main mode measured inside is found again.

The same measurement is reproduced for a sub-zone directly downstream of the rectangular cavity, whose experimental configuration and Fourier transforms in the two zones are compared, in Figs. 5(a) and 5(b), respectively. As suggested by the temporal measurements in the previous configuration, the non-attenuation of the vibrations implies that the resonance frequency of the cavity is not found in the sub-zone, a sign that these frequencies is indeed trapped there, at least over the time of the measurement.

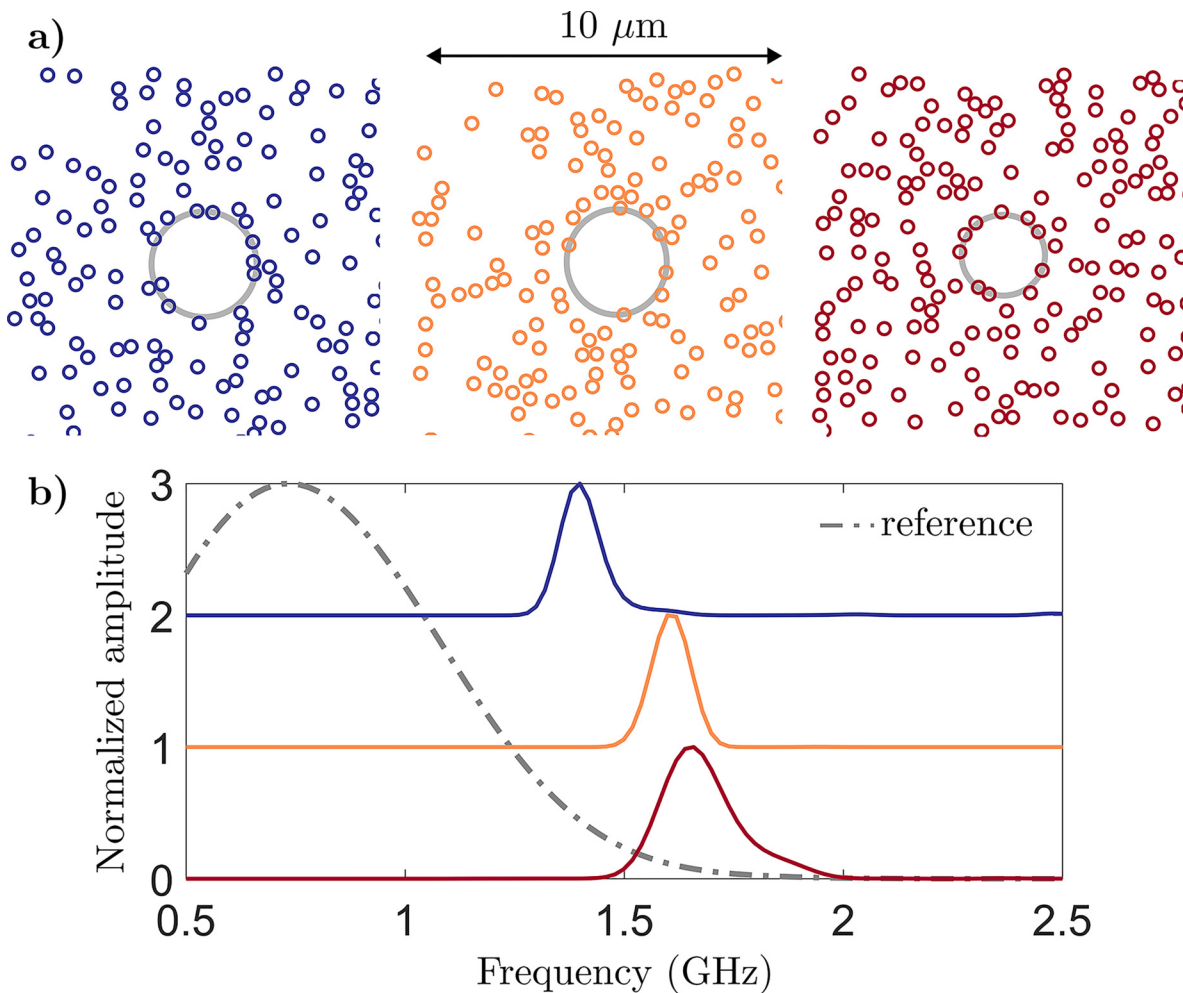
Indeed, as shown by the spectrum of the over-vibrations recorded in the sub-zone, the resonance frequency of the rectangular cavity (denoted by the red arrow) is completely absent. This is confirmed by another experimental configuration in which the excitation is done this time in the direction parallel to the largest dimension of the rectangular cavity, as shown in Fig. 6(a). The spectra of the corresponding measurements recorded in a sub-area before and in the rectangular cavity are compared in Fig. 6(b).

The resonance frequency of the upstream cavity corresponds to a minimum in the rectangular cavity, indicating that this frequency also remains trapped and no longer propagates during the time of the measurement. Given the proximity of the resonance frequencies of these two cavities, the full width at half maximum of the frequency content measured in the rectangular cavity is reduced by a factor 2 from a width FWHM = 0.330.17 GHz from one configuration to the other. The comparison of the experimental results in the two configurations highlights the influence of the direction of excitation on the frequency content of the main mode that will be measured in the cavity, due to the difference of landscape crossed by the wave before getting in the area of interest.

#### IV. NUMERICAL RESULTS

In this section, we present numerical results about harmonic frequency and transient analysis of SAW propagation in the system. In order to have a direct comparison between the measurements and the simulations, calculations have been performed on the same patterns of Al pillars [Figs. 5(a) and 6(a)] that have been manufactured and measured. Specifically, coordinates of the positions of the pillars in the numerical model are extracted from the fabricated samples in a text file, which is then uploaded to the modeling software where the simulated geometry is drawn (using such coordinates). Furthermore, the dimensions of the Al pillars and the film underneath are set as in the experiment, i.e.,  $e_{\text{Al}} = 100$  nm for the latter and  $\varphi = 320$  nm and  $h = 200$  nm, for the diameter and height of the pillars, respectively. Figures 7(a) and 7(b) show the configurations of the numerical simulations: the source load (blue spot) is placed about  $10 \mu\text{m}$  from the two free surfaces in the same way as for the experimental measurements, with the red spots

16 May 2024 13:35:41



16 May 2024 13:35:41

**FIG. 3.** (a) Close environment of three randomly generated cavities highlighted by the gray circles. The size of the cavities in the direction of propagation of the wave are 2.8, 2.4, and 2  $\mu\text{m}$ . (b) Normalized amplitude of the Fourier transform of the signal measured inside the cavities 0.5 ns after the passage of the wavefront that propagates over 10  $\mu\text{m}$  between the pump and the probe. The curves are vertically shifted for the sake of clarity. The reference corresponds to the spectral content of the elastic wave without any scatterers.

corresponding to the measurement points. It should be mentioned that the first geometry [Fig. 7(a)] mimics the experimental configuration in Fig. 5(a), where the source load is facing the longer side of the rectangular cavity, while the second [Fig. 7(b)] simulates the experimental structure in Fig. 6(a) when the source faces its smaller side. These two models help to explore, numerically, the effect of the excitation source direction relative to the cavity investigated experimentally.

We refer to these configurations throughout this section, respectively, as the perpendicular [Fig. 7(a)] and the parallel [Fig. 7(b)] configurations. Let us mention that for the numerical modeling, we employ the finite element method using Comsol Multiphysics. Specifically, we solve for the scattered displacement field  $\mathbf{u}_s = \mathbf{u} - \mathbf{u}_0$  based on the solid mechanic module, where the

vectors  $\mathbf{u}$  and  $\mathbf{u}_0$  correspond to the field in the presence and absence of the pillars, respectively. This is performed by solving for  $\mathbf{u}$  and  $\mathbf{u}_0$  in two sequential steps, which enables to retrieve  $\mathbf{u}_s$ . Strictly speaking, the phase difference between  $\mathbf{u}$  and  $\mathbf{u}_0$  should be taken into account to have the scattered field, that is why we will rather determine the normalized norm of such a field, namely,  $\|\mathbf{u}_s\|$ . The excitation source is a boundary load applied on a circular area whose extension is about  $0.5 \mu\text{m}^2$  in order to mimic the experimental pump; the load is set to vibrate vertically along the  $z$ -axis, namely,  $\mathbf{F}_0 = F_0 e^{i2\pi f} \mathbf{z}$ , where  $f_r \in [1-2.1]$  GHz is the harmonic frequency. Note that the load transverse component of the field is giving rise to the propagating SAW. The substrate is thick enough  $e_{\text{SiO}_2} = 8 \mu\text{m}$  not to be disturbed by the volume waves that are also generated, but also so that the simulation time remains

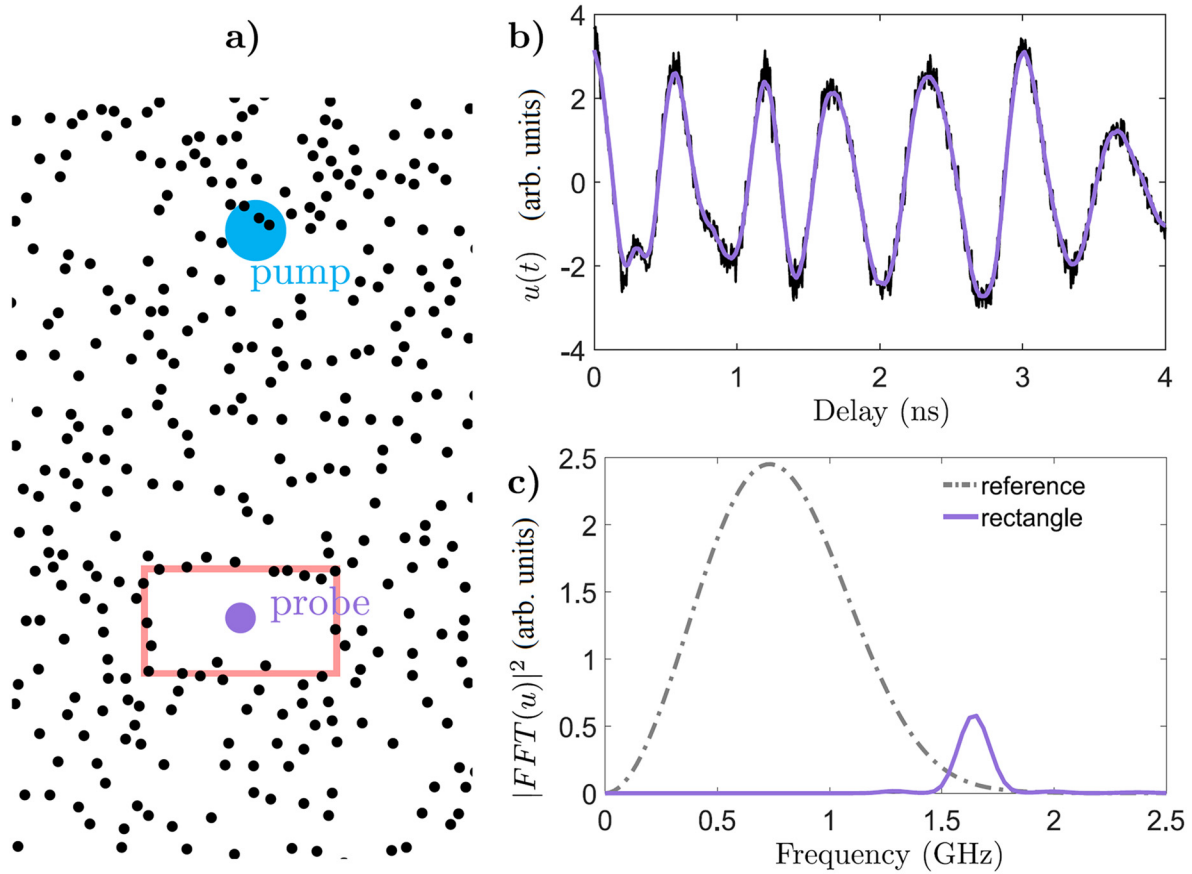


**FIG. 4.** (a) Configuration of the measurement: the pump (blue) and the probe (purple) are separated by  $10\ \mu\text{m}$ . The red rectangle highlights the cavity most studied in this work. (b) Out-of-plane displacement  $u$  measured over 4 ns, directly inside the cavity 0.5 ns after the passage of the elastic wavefront. (c) Spectral content of the vibrations measured inside the cavity.

16 May 2024 13:35:41

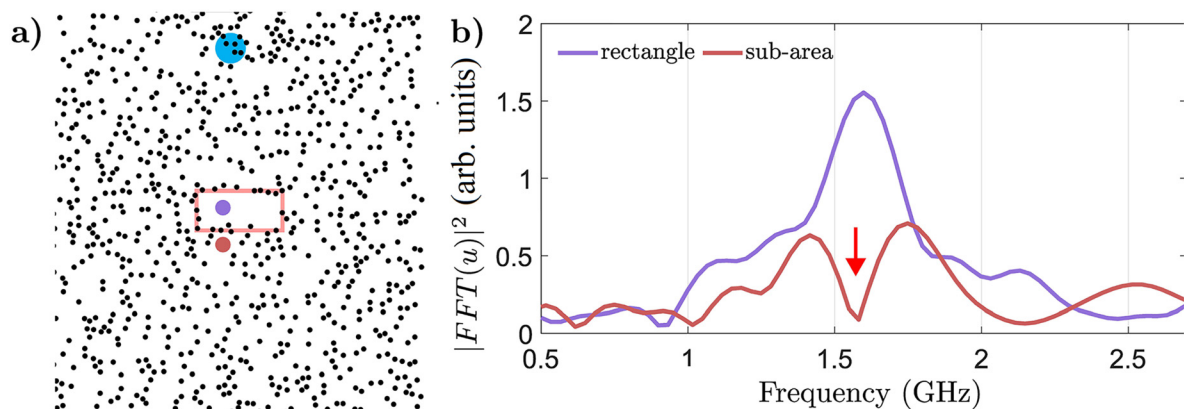


**FIG. 5.** (a) Experimental configuration of the measurement, where the distance between the pump and the probe inside the rectangular cavity is fixed at  $10\ \mu\text{m}$ . (b) Comparison of the Fourier transform between the signal measured inside the rectangular cavity (purple) and in the sub-area (red), 0.5 ns after the passage of the wavefront. The color of the curves corresponds to the color of the probes. The red arrow indicates the resonant frequency of the rectangular cavity.



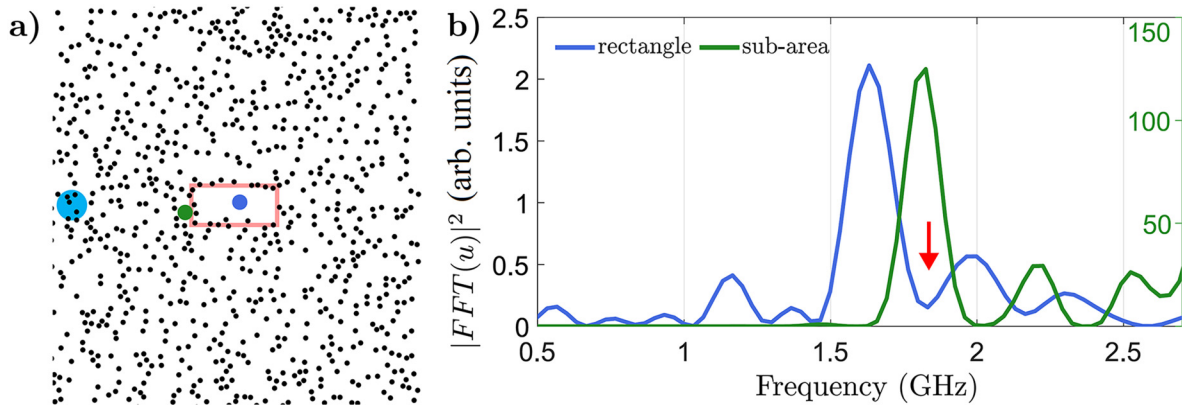


**FIG. 6.** (a) Configuration of the pump-probe measurements such that the distance between the pump and the probe is set at  $10\ \mu\text{m}$ . (b) Comparison of the Fourier transform between the signal measured inside the rectangular cavity (blue) and the in sub-area (green)  $0.5\ \text{ns}$  after the passage of the wave. The colors of the curves correspond to those of the probes. The red arrows indicate the resonant frequencies of the sub-area before the rectangular cavity.

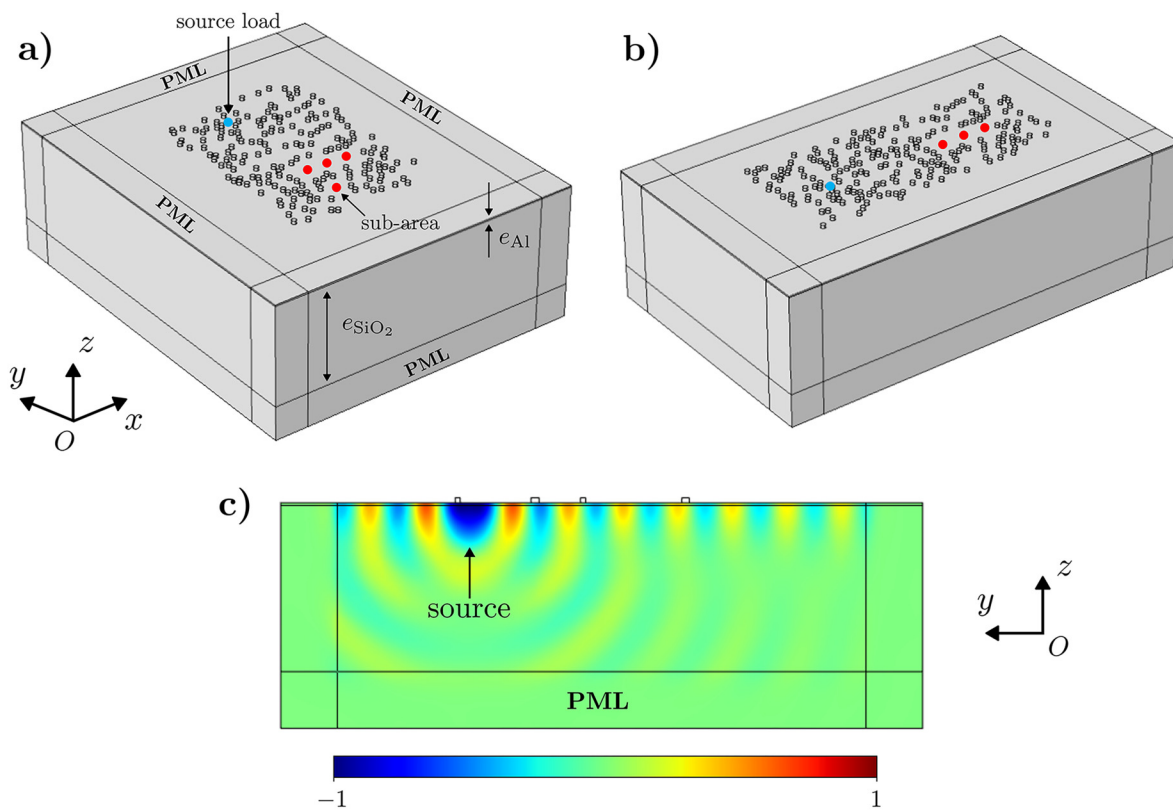


**FIG. 7.** Geometry model of the randomly generated distribution of pillars. (a) Configuration set when the source load faces the longest side of the area free of pillars. (b) Same as (a), but when the source is in front of the short side of the area. Blue and red spots highlight the source load and the probes registering the propagating wave spectrum. The geometrical parameters are  $e_{\text{SiO}_2} = 8\ \mu\text{m}$  for the substrate and  $e_{\text{Al}} = 100\ \text{nm}$  for the Al film, while the dimensions of the pillars are set as in the experiment. The side boundaries of the structures [of (a) and (b)] are terminated with perfect matched layers (PMLs), which are absorbing boundary conditions that eliminate unphysical reflections, while their upper boundaries are set free. (c) Transverse component of the displacement field  $w$  map at  $f_r = 1.48\ \text{GHz}$ , plotted within a  $Oyz$ -cut plane at the middle of the system depicted in (a). The color scale represents the normalized out-of-plane component of the displacement  $w$ .

16 May 2024 13:35:41

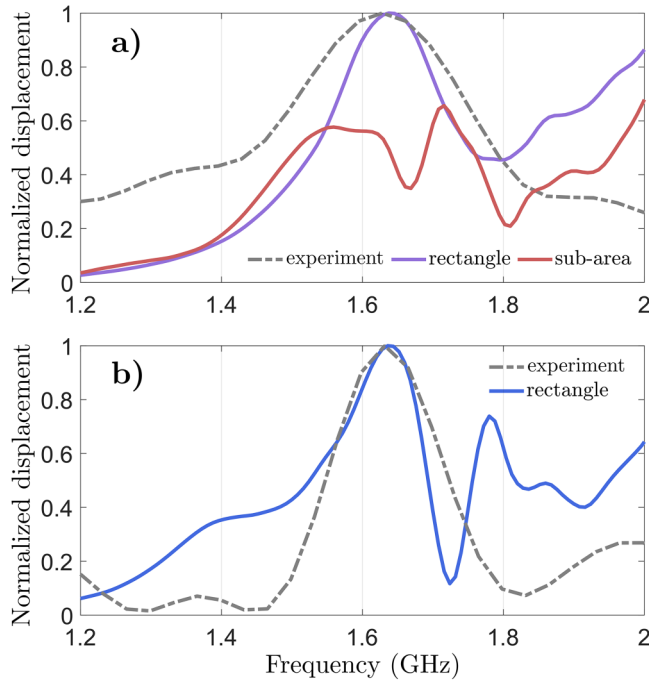


**FIG. 8.** Normalized displacements of the scattered field  $\|w_s\|$  vs frequency for (a) perpendicular and (b) parallel configurations. The spectrum for the rectangle is the average between the three probes in the corresponding area while the spectrum registered in the sub-area is for only one probe, as highlighted by the red spots in Figs. 7(a) and 7(b). These are overlaid by the experimental results, represented as dashed-dotted lines.

reasonable. That is also why the calculations were performed on a reduced number of pillars compared to the experimental configuration since only  $\sim 150$  scatterers have been implemented.

Despite this significant difference in the number of pillars, we emphasize that this is still sufficient to reproduce the effects experimentally observed. Both studied geometries are surrounded by perfect matched layers (PMLs) to absorb outgoing waves without reflections. As for the mesh, we used free tetrahedral finite elements with 5–6 elements per diameter and height of each pillar and 4 elements per wavelength along the top surface. In PMLs on the other side, a swept mesh is applied with 6 elements per wavelength, while in the remaining bulk, a coarser mesh is set. We use second-order polynomial functions within each finite element to approximate the field solved for, which ensure accurate results. In Fig. 7(c), we present the field  $u$  transverse component map in a  $Oyz$ -cut plane of the system (near the middle) sketched in Fig. 7(a), at  $f_r = 1.48$  GHz; one notes the effective excitation of the SAW confined near the top surface. In order to investigate the interaction between the Al scatterers and the incident SAW within the rectangular free surface, we simulate the spectrum of the transverse component of  $u_s$  norm, namely,  $\|w_s\|^2 = \|w - w_0\|^2$ , with  $w$  and  $w_0$ , the transverse components of the fields  $u$  and  $u_0$ , respectively.

In Figs. 8(a) and 8(b), we show simulated spectra for perpendicular and parallel configurations, overlaid by the experimental measurements in the rectangle for the perpendicular case as a dotted line. The numerical results obtained for the rectangle have been averaged over three probe positions, while the result for the sub-area that is obtained for one probe only and is normalized by the spectra in the rectangular cavity. The positions of the numerical probes are highlighted by the red spots in Fig. 7. This comparison shows a good agreement between the spectra measured and

16 May 2024 13:35:41

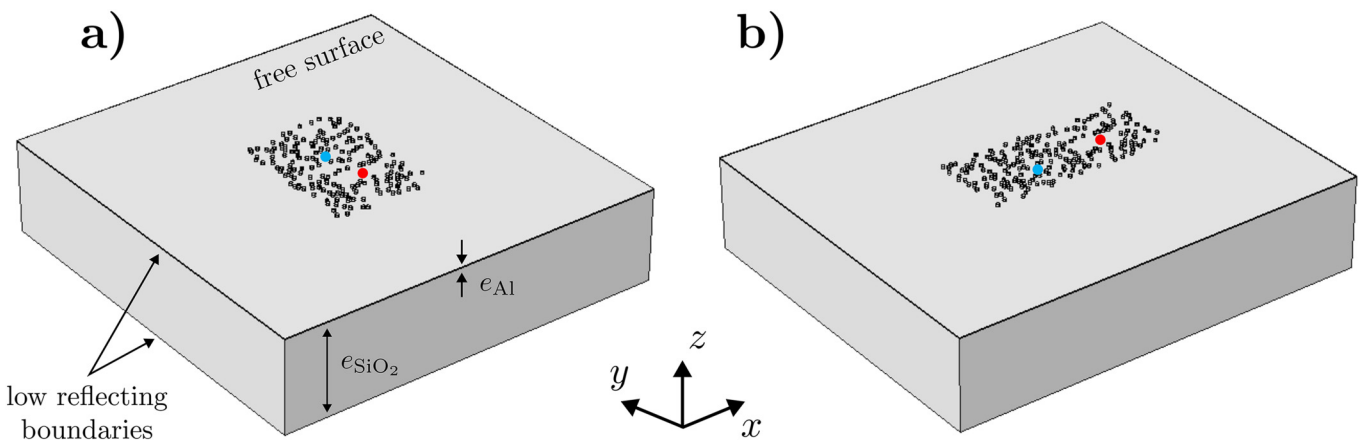


**FIG. 9.** (a), (b) Depiction of the extended geometry model for the perpendicular and parallel main dimensions of the rectangle, respectively. A low reflection boundary condition is applied on the side and the bottom of the geometry while the upper surface is set free. The dimensions of the sample are the same as those in Fig. 7. Blue and red spots highlight the source load and the probe registering the temporal signal.

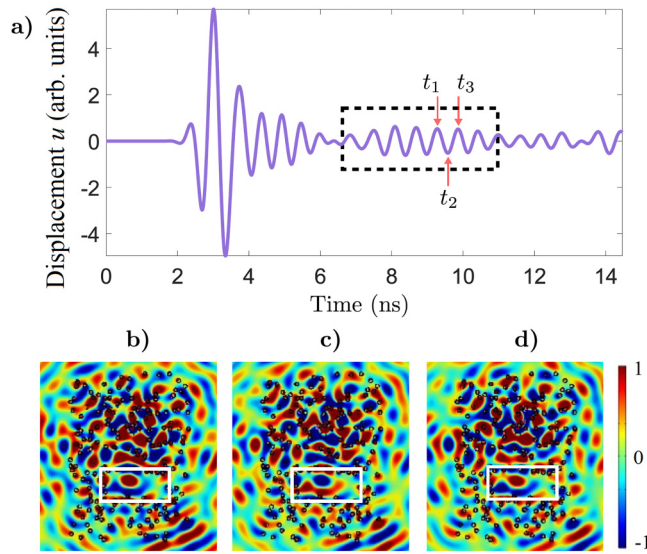


**FIG. 10.** (a) Registered time signal inside the rectangle free surface indicated by the red spot in Fig. 9(a). The dotted rectangle indicates the over vibrations caused by the wave's passage through the free surface over time, before reflections from the edges of the calculation domain reach it again. (b)–(d) Snapshots of the out-of-plane displacement at three different times indicated by the red arrows on the time signal:  $t_1 \sim 2.7$ ,  $t_2 \sim 3$ , and  $t_3 \sim 3.3$  ns after the passage of the SAW through the free area, which is highlighted by a white rectangle. The color scale represents the normalized out-of-plane component of the displacement  $w$ .

simulated inside the rectangle in terms of spectral content since the experimental and calculated main frequencies trapped inside are the same, both for the two configurations. One can notice that the FWHM of the signal measured is a bit wider because the spectral resolution is constrained in that case compared to the numerical simulations where it can easily be tuned by changing the sweep in the frequency domain. In the same way that has been demonstrated by the experimental results of Fig. 5(b), the main frequency present inside the rectangle is lacking in the sub-area, meaning that the former is effectively trapping the wavelengths that match its characteristic dimension.

We now focus on the simulation of transient SAW propagation over time in the structure depicted in Figs. 9(a) and 9(b). For that matter, we basically use the same geometry models sketched in Figs. 7(a) and 7(b), except that the boundary condition's type is changed to truncate the simulated system. As a matter of fact, unlike the frequency domain, PMLs do not absorb well the outgoing waves in the time domain which might perturb the propagating waves in the structure due to spurious reflections. Instead, we increase the size of the free surface surrounding the pillars and employ a low reflecting boundary condition to terminate the geometry on the side and bottom.

The results of the time domain simulation for the perpendicular configuration are given in Fig. 10(a). The SAW reaches the pillar's free surface at  $\sim 2$  ns and leaves it at  $\sim 6.6$  ns, highlighting the over-vibrations within it up to 11 ns, at which point, they are

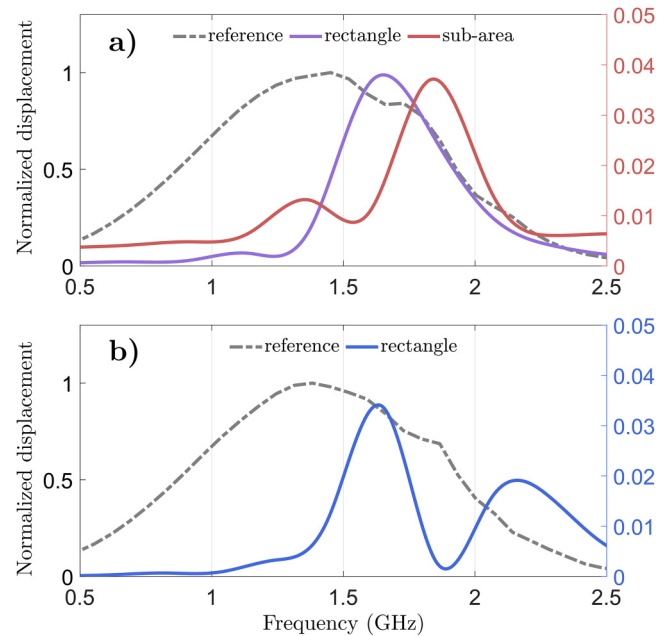


**FIG. 11.** Fourier transform of the over vibrations after the passage of the wave through (a) the rectangle and the sub-area for configuration in Figs. 9(a) and 9(b) through the rectangle for configuration in Fig. 9(b). The reference (dashed-dotted line) corresponds to the spectral content of the initial signal that is launched into the random distribution of pillars. The left vertical scale represents the spectral content of the signal numerically generated, while the right one is the distribution of scatterers, normalized by the reference signal outside the distribution.

disturbed by reflections from the edge of the calculation domain. Enlarging the geometry of the domain would then allow us not to be disturbed by these parasitic reflections, in order to determine the duration of the corresponding over-vibrations, but would lead to a calculation time that would be far too long and not necessary for the needs of this study. For this reason, we have focused solely on the over-vibration zone between 6.6 and 11 ns, which is sufficient for the comparison with the experimental results.

The corresponding out-of-plane displacement fields are shown in Figs. 10(b)–10(d) for three different over-vibrating states, labeled as  $t_1$ ,  $t_2$ , and  $t_3$ , i.e., 2.7, 3, and 3.3 ns after the passage of the SAW through the free pillar areas, respectively. These images reveal changes in the vibrational landscape as a function of time and, in particular, a field phase inversion from one instant to the next, suggesting that the free surface vibrates at a defined frequency, as has been demonstrated experimentally. These observations are also confirmed for the parallel configuration, as can be seen in Figs. 12(a)–12(d) in the Appendix. Performing the Fourier transform over the over-vibrating region highlighted in the time domain calculations allows us to retrieve the main frequency trapped inside the free area for both configurations. Both Figs. 11(a) and 11(b) (perpendicular and parallel configurations) confirm the experimental observations, since despite the wide reference spectral content launched in the

sample (in the absence of pillars), only a small proportion of the vibrations persist in the zone investigated after the wavefront has passed through it.

It is worth mentioning that for the parallel configuration [Fig. 11(b)], a small frequency band is seen in the cavity spanning  $\sim 1.9$ – $2.5$  GHz. Such a band is observed due to the fact that the excited Gaussian pulse numerically is centered at 1.4 GHz, which includes frequencies up to  $\sim 2.5$  GHz. This was meant in order to highlight the resonance near 1.6 GHz in the cavity. Besides, according to the dispersion curves of the system where the pillars form a squared array [see Fig. 12(a)], with a lattice parameter of  $\sim 0.65$   $\mu\text{m}$  corresponding roughly to the mean distance between pillars in the disordered structure, these modes possibly relate to the bending and compressional modes [Fig. 12(b)] of coupled pillars around the cavity. In fact, given that the compression mode is at  $\sim 2.3$  GHz, probably, the latter radiates some of the energy mostly in this mode toward the cavity. On the other hand, regarding the calculations in the frequency domain, an excellent agreement is found between the main frequencies trapped inside the rectangle for both numerical and experimental configurations. The same absence of this resonant frequency in the sub-area indicates the effective trapping of the spectral content of the SAW that matches the characteristic dimensions of the free area inside the random distribution of scatterers.

## V. CONCLUSION

In this study, we have been focusing on the propagation of high frequency surface acoustic waves through a random distribution of Al scatterers obeying a Poisson statistic. To this end, a pump and probe spectroscopy setup has been used, as it enables us to study the spatial and temporal dynamics of disordered metasurfaces directly from within the inside of the distribution, with a micrometric spatial resolution. Wide-plane images of the acoustic wave's out-of-plane displacement field suggest that, as the SAW propagates, it gives up some of its energy to the random distribution of pillars. This energy is mainly confined inside randomly formed pillar-free zones. The versatility of the experimental setup enabled us to demonstrate that, for simple geometries such as circular shapes, the wavelengths of the confined acoustic energy are directly related to their characteristic dimensions. Further measurements have been carried out on a rectangular geometry and its immediate surroundings, confirming the conclusions reached on circular geometries. In addition, this geometry has been particularly interesting as it acts as a real acoustic trap, since the wavelengths corresponding to its characteristic dimensions no longer propagate through the structure. All these experimental observations were also studied numerically using Comsol Multiphysics simulation software, with time and frequency solvers that were complementary to this study. Despite the significant difference between the number of pillars measured and simulated, the same effects were observed, with a very good correspondence between experience and theory. In particular, the effect of trapping acoustic energy in the distribution was found for the same frequencies. The reported findings shall help to investigate the enhanced coupling between co-localized surface phonons and photons in the metasurface, with application in acousto-optical modulation or ultrasensitive sensing.

## ACKNOWLEDGMENTS

This work was supported by the French National Research Agency ANR, as part of the project "RANDOM" (Reference No. ANR-19-CE24-0014) and by the European Commission as part of the project "DYNAMO" (HORIZON-EIC-2021-PATHFINDEROPEN-01 Project ID 101046489). The authors would like to thank Eric Charron for his technical assistance.

## AUTHOR DECLARATIONS

### Conflict of Interest

The authors have no conflicts to disclose.

### Author Contributions

**Thibault Deletang:** Investigation (equal); Writing – original draft (equal). **Adnane Noual:** Investigation (supporting); Software (lead); Writing – original draft (equal). **Bernard Bonello:** Investigation (equal); Methodology (equal); Writing – review & editing (equal). **Roman Buisine:** Investigation (supporting). **Yan Pennec:** Investigation (equal); Project administration (lead); Software (supporting). **Bahram Djafari-Rouhani:** Funding acquisition (supporting); Investigation (equal); Writing – original draft (equal).

## DATA AVAILABILITY

The data that support the findings of this study are available from the corresponding author upon reasonable request.

## APPENDIX: SIMULATION OF THE DISPLACEMENT FIELD IN THE PARALLEL CONFIGURATION

We present in Fig. 12(a), the simulated signal corresponding to the out-of-plane displacement field ( $t$ ) inside the cavity set in the parallel configuration. Similar to the perpendicular configuration, the SAW arrives into the cavity around  $\sim 2$  ns and leaves at  $\sim 6$  ns; over-vibrations remain trapped inside until roughly 11 ns. In Figs. 12(b)–12(d), we show snapshots of the field ( $t$ ) inside the cavity highlighting the over-vibrations states, at  $t_1 \sim 2.3$ ,  $t_2 \sim 2.6$ , and  $t_3 \sim 2.9$  ns, where we note the field phase inversion from one instant to the next, confirming the defined frequency at which the free surface vibrates in the parallel configuration in accord with the experimental data.

In order to provide a qualitative explanation of the observed frequency band spanning roughly the domain  $\sim 1.9$ – $2.4$  GHz, we have plotted in Fig. 12(e) the simulated dispersion curves of the metasurface using the finite element method such that the pillars are organized in a squared array with a lattice parameter  $a = 0.65$   $\mu\text{m}$ . This value matches approximately the mean distance between the pillars in the fabricated sample. Bloch boundary conditions are used to mimic periodicity in the structure. One notes at the Brillouin zone edge that two degenerate bending modes of the pillar fall at  $\sim 1.79$  GHz, while compressional and torsional modes occur at 2.3 GHz and 2.67 GHz. Hence, the disordered metasurface coupled pillars near or around the cavity vibrating in such modes, especially, the compressional mode ( $\sim 2.3$  GHz), probably radiate some of the energy in the cavity that we observe in Fig. 10(b). It should be indicated that this band centered around  $\sim 2.25$  GHz is clearly favored by the parallel cavity set as it is not seen in the

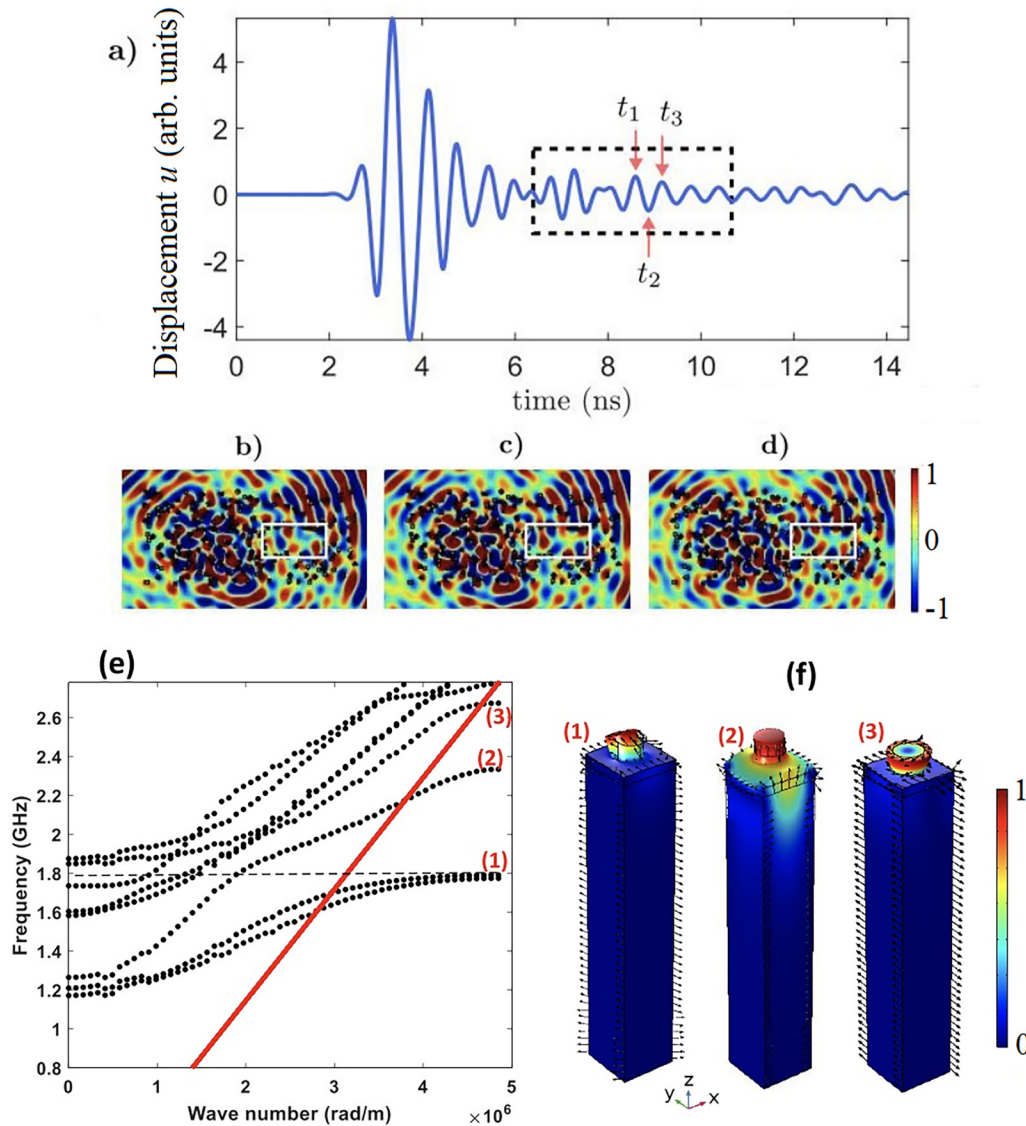


**FIG. 12.** (a) Registered time signal inside the rectangle free surface indicated by the red spot in Figs. 9(b), 9(b), 9(c), and 9(d). Snapshots of the out-of-plane displacement at three different instants indicated by the red arrows on the time signal:  $t_1 \sim 2.3$ ,  $t_2 \sim 2.6$ , and  $t_3 \sim 2.9$  ns after the passage of the SAW through the free area, which is highlighted by a white rectangle. The color scale represents the normalized out-of-plane component of the displacement  $w$ . (e) Dispersion curves of the metasurface when the pillars are ordered in a squared array, with the lattice parameter  $a = 0.65 \mu\text{m}$ . (f) Displacement field norm map within a unit cell for the modes referred to as (1), (2), and (3) in (e). These correspond to the bending, torsional, and compressional resonances of the pillar, respectively. The color scale represents the normalized displacement field norm.

perpendicular configuration [Fig. 10(a)], which confirms the hint that the landscape encountered by the incident wave influences the observed modes inside the cavity.

## REFERENCES

<sup>1</sup>S. Yu, C.-W. Qiu, Y. Chong, S. Torquato, and N. Park, “Engineered disorder in photonics,” *Nat. Rev. Mater.* **6**, 226–243 (2021).

<sup>2</sup>Y. Cui, K. H. Fung, J. Xu, H. Ma, Y. Jin, S. He, and N. X. Fang, “Ultrabroadband light absorption by a sawtooth anisotropic metamaterial slab,” *Nano Lett.* **12**, 1443–1447 (2012).

<sup>3</sup>J. Mei, G. Ma, M. Yang, Z. Yang, W. Wen, and P. Sheng, “Dark acoustic metamaterials as super absorbers for low-frequency sound,” *Nat. Commun.* **3**, 756 (2012).

<sup>4</sup>P. A. Belov, Y. Hao, and S. Sudhakaran, “Subwavelength microwave imaging using an array of parallel conducting wires as a lens,” *Phys. Rev. B* **73**, 033108 (2006).

- <sup>5</sup>J. B. Pendry, A. Aubry, D. R. Smith, and S. A. Maier, "Transformation optics and subwavelength control of light," *Science* **337**, 549, (2012).
- <sup>6</sup>M. Oudich, X. Zhou, and M. Badreddine Assouar, "General analytical approach for sound transmission loss analysis through a thick metamaterial plate," *J. Appl. Phys.* **116**, 193509 (2014).
- <sup>7</sup>O. Leseur, R. Pierrat, and R. Carminati, "High-density hyperuniform materials can be transparent," *Optica* **3**, 763 (2016).
- <sup>8</sup>A. Rohfritsch, J.-M. Conoir, T. Valier-Brasier, and R. Marchiano, "Impact of particle size and multiple scattering on the propagation of waves in stealthy-hyperuniform media," *Phys. Rev. E* **102**, 053001 (2020).
- <sup>9</sup>J. B. Pendry, D. Schurig, and D. R. Smith, "Controlling electromagnetic fields," *Science* **312**, 1780–1782, (2006).
- <sup>10</sup>M. Farhat, S. Enoch, S. Guenneau, and A. B. Movchan, "Broadband cylindrical acoustic cloak for linear surface waves in a fluid," *Phys. Rev. Lett.* **101**, 134501 (2008).
- <sup>11</sup>C. He, X. Ni, H. Ge, X.-C. Sun, Y.-B. Chen, M.-H. Lu, X.-P. Liu, and Y.-F. Chen, "Acoustic topological insulator and robust one-way sound transport," *Nat. Phys.* **12**, 1124–1129 (2016).
- <sup>12</sup>P. St-Jean, V. Goblot, E. Galopin, A. Lemaître, T. Ozawa, L. Le Gratiet, I. Sagnes, J. Bloch, and A. Amo, "Lasing in topological edge states of a one-dimensional lattice," *Nat. Photonics* **11**, 651–656 (2017).
- <sup>13</sup>P. W. Anderson, "Absence of diffusion in certain random lattices," *Phys. Rev.* **109**, 1492–1505 (1958).
- <sup>14</sup>A. Lagendijk, B. V. Tiggelen, and D. S. Wiersma, "Fifty years of Anderson localization," *Phys. Today* **62**(8), 24–29 (2009).
- <sup>15</sup>S. John, "Electromagnetic absorption in a disordered medium near a photon mobility edge," *Phys. Rev. Lett.* **53**, 2169–2172 (1984).
- <sup>16</sup>H. Hu, A. Strybulevych, J. H. Page, S. E. Skipetrov, and B. A. van Tiggelen, "Localization of ultrasound in a three-dimensional elastic network," *Nat. Phys.* **4**, 945–948 (2008).
- <sup>17</sup>D. S. Wiersma, M. P. van Albada, B. A. van Tiggelen, and A. Lagendijk, "Experimental evidence for recurrent multiple scattering events of light in disordered media," *Phys. Rev. Lett.* **74**, 4193–4196 (1995).
- <sup>18</sup>F. Riboli, P. Barthelemy, S. Vignolini, F. Intonti, A. De Rossi, S. Combrie, and D. S. Wiersma, "Anderson localization of near-visible light in two dimensions," *Opt. Lett.* **36**, 127 (2011).
- <sup>19</sup>A. Cazé, R. Pierrat, and R. Carminati, "Strong coupling to two-dimensional Anderson localized modes," *Phys. Rev. Lett.* **111**, 053901 (2013).
- <sup>20</sup>D. S. Wiersma, "Disordered photonics," *Nat. Photonics* **7**, 188–196 (2013).
- <sup>21</sup>F. Riboli, N. Caselli, S. Vignolini, F. Intonti, K. Vynck, P. Barthelemy, A. Gerardino, L. Balet, L. H. Li, A. Fiore, M. Gurioli, and D. S. Wiersma, "Engineering of light confinement in strongly scattering disordered media," *Nat. Mater.* **13**, 720–725 (2014).
- <sup>22</sup>C. W. Hsu, S. F. Liew, A. Goetschy, H. Cao, and A. Douglas Stone, "Correlation-enhanced control of wave focusing in disordered media," *Nat. Phys.* **13**, 497–502 (2017).
- <sup>23</sup>A. Canaguier-Durand, R. Pierrat, and R. Carminati, "Cross density of states and mode connectivity: Probing wave localization in complex media," *Phys. Rev. A* **99**, 013835 (2019).
- <sup>24</sup>F. Zhang, F. Tang, X. Xu, P.-M. Adam, J. Martin, and J. Plain, "Influence of order-to-disorder transitions on the optical properties of the aluminum plasmonic metasurface," *Nanoscale* **12**, 23173–23182 (2020).
- <sup>25</sup>F. Sgrignuoli, S. Torquato, and L. Dal Negro, "Subdiffusive wave transport and weak localization transition in three-dimensional stealthy hyperuniform disordered systems," *Phys. Rev. B* **105**, 064204 (2022).
- <sup>26</sup>R. Sainidou, N. Stefanou, and A. Modinos, "Widening of phononic transmission gaps via Anderson localization," *Phys. Rev. Lett.* **94**, 205503 (2005).
- <sup>27</sup>E. Metin Akinoglu, T. Sun, J. Gao, M. Giersig, Z. Ren, and K. Kempa, "Evidence for critical scaling of plasmonic modes at the percolation threshold in metallic nanostructures," *Appl. Phys. Lett.* **103**, 171106 (2013).
- <sup>28</sup>N. Papasimakis, V. A. Fedotov, Y. H. Fu, D. P. Tsai, and N. I. Zheludev, "Coherent and incoherent metamaterials and order-disorder transitions," *Phys. Rev. B* **80**, 041102 (2009).
- <sup>29</sup>A. A. Fernández-Marín, J. A. Méndez-Bermúdez, J. Carbonell, F. Cervera, J. Sánchez-Dehesa, and V. A. Gopar, "Beyond Anderson localization in 1D: Anomalous localization of microwaves in random waveguides," *Phys. Rev. Lett.* **113**, 233901 (2014).
- <sup>30</sup>N. Fernez, L. Burgnies, D. Dereudre, D. Lippens, and E. Lheurette, "Poisson distributions in disordered metamaterials absorbers," *J. Appl. Phys.* **125**, 213106 (2019).
- <sup>31</sup>E. El Shamy, J. Jaeck, R. Haïdar, and P. Bouchon, "Light scattering by correlated disordered assemblies of nanoantennas," *Appl. Phys. Lett.* **115**, 041103 (2019).
- <sup>32</sup>A. C. Hladky-Hennion, J. O. Vasseur, S. Degraeve, C. Granger, and M. de Billy, "Acoustic wave localization in one-dimensional Fibonacci phononic structures with mirror symmetry," *J. Appl. Phys.* **113**, 154901 (2013).
- <sup>33</sup>J. Flores, L. Gutiérrez, R. A. Méndez-Sánchez, G. Monsivais, P. Mora, and A. Morales, "Anderson localization in finite disordered vibrating rods," *Eur. Phys. Lett.* **101**, 67002 (2013).
- <sup>34</sup>A. Noul, R. Akiki, Y. Pennec, E. H. El Boudouti, and B. Djafari-Rouhani, "Surface acoustic waves-localized plasmon interaction in pillared phononic crystals," *Phys. Rev. Appl.* **13**, 024077 (2020).
- <sup>35</sup>O. Matsuda, M. C. Larciprete, R. Li Voti, and O. B. Wright, "Fundamentals of picosecond laser ultrasonics," *Ultrasonics* **56**, 3–20 (2015).
- <sup>36</sup>J. H. Page, P. Sheng, H. P. Schriemer, I. Jones, X. Jing, and D. A. Weitz, "Group velocity in strongly scattering media," *Science* **271**, 634–637, (1996).